Efficient prediction of propeller noise in non-axial uniform inflow conditions

Yunus, F.; Casalino, Damiano; Romani, Gianluca; Snellen, Mirjam

Important note
To cite this publication, please use the final published version (if applicable).
Please check the document version above.

Efficient prediction of propeller noise in non-axial uniform inflow conditions

Furkat Yunus [a], [*], Damiano Casalino [b], Gianluca Romani [b], Mirjam Snellen [a]

[a] *Control and Operation Department, Delft University of Technology, Delft 2629HS, the Netherlands*
[b] *Dassault Systemes Deutschland GmbH, Germany*

ARTICLE INFO

ABSTRACT

This paper investigates the prediction accuracy and time efficiency of two distinct low-fidelity methods for predicting the tonal and broadband noise of a drone rotor in axial and non-axial inflow conditions. These are both derived from an aerodynamic rotor model based on the blade element momentum theory, respectively coupled with a time- and a frequency-domain solution of the Ffowcs Williams-Hawkings integral equation applied to a radial distribution of acoustically compact and non-compact sources. Experimental data and scale-resolving lattice-Boltzmann/very-large eddy simulation results for a two-bladed small unmanned aerial system in transitional boundary layer conditions are used to validate the low-fidelity approaches. Comparison between low-fidelity, high-fidelity and experimental results reveal that the underlying sound generation mechanisms are accurately modeled by the low-fidelity methods, which therefore constitute a valid tool for the preliminary design of quiet drone rotors and for the estimation of the community noise impact of drone operations.

1. Introduction

Recent advancements in battery technology and the effective deployment of distributed electric propulsion systems in various unmanned aerial vehicles and urban air mobility platforms have highlighted the growing adoption of multi-propeller configurations as the preferred propulsion method. While these innovations offer significant performance advantages, they also pose a substantial challenge: community noise impact, particularly during low-altitude operations in densely populated urban settings. This noise concern represents a key obstacle to the broader integration and future deployment of air mobility and drone operations within urban environments.

Propeller noise spectra are characterized by the presence of both tonal and broadband components. Tonal noise arises from deterministic sources, including thickness noise, which is due to the fluid displaced by the moving blades, steady-loading noise, which is caused by the steady forces acting on the blades, and unsteady-loading noise, which primarily results from local distortions in the inflow or non-axial inflow conditions, say when the propeller shaft is not aligned with the incoming airflow. In non-axial inflow, each blade experiences periodic variations in the local angle of attack, leading to fluctuations in blade loading that generate periodic unsteady-loading noise at harmonics of

the blade-passage frequency (BPF) [1]. This situation commonly occurs in maneuvering conditions, such as during take-off or landing of propeller-driven aircraft, and during vertical/horizontal flight conversion of vertical takeoff and landing (VTOL) vehicles. In both cases, the noise impact on the exposed communities must be properly evaluated and regulated, as recently discussed in [2]. This study focuses on the prediction of unsteady-loading noise generated under non-axial inflow conditions, assuming a uniform inflow without local distortions. Broadband noise, on the other hand, includes turbulence ingestion noise, blade-wake interaction noise, and blade self-noise. The latter originates from turbulent pressure fluctuations in the boundary layer or from separations and vortex shedding. Most notably, self-noise is due to the scattering of turbulent boundary layer fluctuations by the trailing edge [3]. This is the only broadband noise generation mechanism considered in the present study.

High-fidelity (H-F) numerical approaches, which combine computational fluid dynamics (CFD) simulations with the Ffowcs-Williams Hawkings (FW-H) acoustic analogy, are widely used to study propeller noise. Among these methods, the lattice-Boltzmann/very large eddy simulation (LB/VLES) method, has been applied to different classes of rotor aeroacoustic problems, including small propellers for unmanned aerial systems [4–7], larger propellers for urban air mobility vehi-

Nomenclature

B	number of blades		T	thrust
c	blade chord		V_∞	free stream velocity
c_0	sound speed		V_A	axial component of V_∞
C_d	2D drag coefficient		V_Z	in-plane component of V_∞
C_l	2D lift coefficient		V_a	sectional axial velocity
$C_{\partial_r T}$	$\partial_r T/(\rho n^2 D^3)$		V_i	sectional induced velocity
$C_{\partial_r Q}$	$\partial_r Q/(\rho n^2 D^4)$		V_t	sectional tangential velocity
D	propeller diameter		W	sectional relative velocity
J	advance ratio, $J = V_\infty/(nD)$		α	airfoil angle of attack
M_∞	free stream Mach number		α_P	propeller angle of attack
m	acoustic harmonic number		β	blade twist angle
n	rotational speed, $n = \Omega/2\pi$		ϕ	inflow angle
Q	torque		ψ	azimuthal angle
Re	Reynolds number		$\partial_r T$	sectional thrust
R	blade radius		$\partial_r Q$	sectional torque
r	radial coordinate		ρ	fluid density
Δr	width of a blade element		Ω	rotational frequency

cles [8], and electric passenger-aircraft [9], under different operating conditions, ranging from hovering [4–7] to forward flight [9,10], and in non-axial inflow conditions [5,7]. H-F simulations become prohibitively expensive when evaluating propeller noise under several non-axial inflow conditions, such as during takeoff flight. This is especially challenging when optimizing low-noise flight procedures and trajectories, which often require thousands of simulations across different flight and operating conditions [8]. As a result, there is a growing need for computationally efficient and reliable methods to predict propeller noise for flight mission analysis and community noise assessment.

Low-fidelity (L-F) approaches, on other hand, predict propeller noise by coupling aerodynamic and acoustic models. The accuracy of these L-F methods largely depends on the aerodynamic model used. Among the popular methods, blade element momentum theory (BEMT) is commonly employed for preliminary aerodynamic analysis and rotor design, particularly for propellers and wind turbines. BEMT has proven consistently reliable in producing results that align closely with experimental data, while maintaining low computational costs [4,11,9,12]. However, the BEMT used in these studies assumes a uniform axial inflow and thus cannot account for contributions from unsteady loading of the propeller at incidence. In this study, the BEMT approach is extended to predict unsteady loading on a propeller operating under non-axial uniform inflow. While the current work focuses on isolated rotors, the methodology can be adapted to multi-rotor configurations by incorporating wake induction effects from adjacent rotors, as demonstrated in recent work by Usov et al. [13].

From a theoretical standpoint, the solutions derived from the FW-H equations, which describe the noise radiation resulting from arbitrary motions of surfaces in a fluid, offer a comprehensive approach that considers the effects of various noise generation mechanisms. Notably, formulations such as Farassat 1 and 1A are extensively used to calculate the noise generated by rotating machines, including propellers translating with an incidence in a quiescent medium [14]. As an alternative to these formulations, Ghorbaniasl and Lacor [15] introduced a time-domain moving medium formulation that explicitly considers the aerodynamic and acoustic effects of non-axial inflow with arbitrary direction. In an effort to enhance computational efficiency and applicability from transonic to supersonic tip speeds, Ghorbaniasl et al. [16] later proposed a frequency-domain version of the time-domain moving medium formulation. In the current study, two different BEMT approaches - extended to model unsteady loadings under non-axial inflow conditions - are coupled to a frequency-domain FW-H formulation derived by Ghorbaniasl et al. [16] and a compact monopole/dipole forward-time Farassat's 1A formulation [17], respectively, in order to predict the noise radiated by

propellers at incidence. This represents the first original contribution of this research.

Despite the existence of several L-F approaches, their computational accuracy and efficiency have not been comprehensively examined. To address this gap, the aforementioned two L-F approaches are compared in terms of computational accuracy and runtime against H-F simulation results and wind tunnel measurement data obtained from previous benchmark studies [4,5]. This comparison constitutes the second original contribution of this paper.

The remainder of the paper is organized as follows. In Section 2, an overview of the L-F approaches is presented. The reference propeller and H-F simulation setup are presented in Section 3. The results are discussed in Section 4. Finally, conclusive remarks are reported in Section 5.

2. Overview of low-fidelity methodologies

In this study, two different low-fidelity rotor aeroacoustic solvers are considered: LOPNOR, an in-house code developed by the leading author, and *Opty∂B*-BEMT/*Opty∂B*-PNOISE, part of the multi-purpose toolkit SIMULIA *Opty∂B*®. Both solvers follow a two-step approach. First, they compute aerodynamic loads and boundary layer properties along the blade span using a BEMT method: LOPNOR incorporates XFOIL [18], while *Opty∂B*-BEMT uses an embedded 2D viscous panel code [4]. Second, they calculate tonal noise by assuming a radial distribution of equivalent thickness and loading noise sources, and trailing-edge noise by means of a semi-analytical formulation based on the boundary layer properties in proximity of the trailing edge. LOPNOR is only able to compute the tonal noise radiation. The aerodynamic and aeroacoustic models used in both solvers are briefly outlined below.

2.1. LOPNOR

The LOPNOR solver is initially validated against H-F simulation results and outdoor measurements [9]. The BEMT approach employed in LOPNOR assumes uniform axial inflow and, therefore, cannot account for unsteady (periodic) loadings from the propeller at incidence. This limitation is addressed by an extended BEMT approach that accounts for the unsteady effects, which will be outlined in the following section.

When a propeller operates in non-axial inflow, the freestream velocity V_∞ is decomposed into two components: V_A along the rotation axis and V_Z in the rotor disk plane, with respect to the propeller incidence angle and rotational axis, as illustrated in Fig. 1. Due to the nonzero incidence angle α_P, both the local velocity and the angle of attack α for each blade section vary with the azimuthal position ψ on the rotor disk.
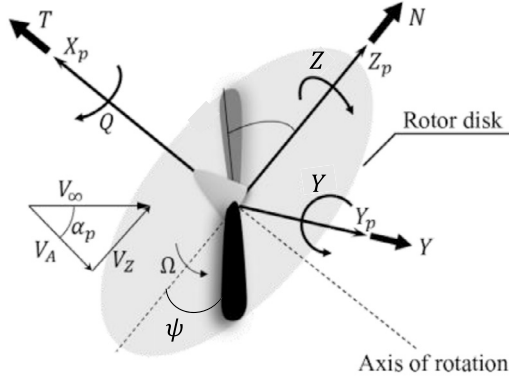
Fig. 1. Illustration of propeller operating in non-axial inflow and propeller coordinate system (adapted from [19]).

Consequently, an imbalance of lift and drag forces occurs on a blade section over a full revolution. These imbalances create a pitching moment Y around the Y_p axis and a rolling moment Z around the Z_p axis. Additionally, $V_A = V_\infty \cos\alpha_P$ reduces the freestream velocity effect in the axial direction, while $V_Z = V_\infty \sin\psi$ introduces a variation in cross flow dependent on the blade azimuthal position, ψ, which will be discussed further below.

As illustrated in Fig. 2, on the advancing side of the propeller, where $0 < \psi < \pi$, the in-plane component of the freestream V_Z aligns with the direction of blade rotation. This alignment increases the tangential velocity at a blade element, expressed as $V_t(\psi) = r\Omega + V_\infty \sin\alpha_P \sin\psi - V_{iT}$, with V_{iT} representing the tangential component of the induced velocity. The axial velocity on the advancing blade side is given by $V_a(\psi) = V_\infty \cos\alpha_P + V_{iA}$ and is independent of ψ. Consequently, the local relative wind speed $W(\psi) = \sqrt{V_a^2 + V_t^2}$ increases. The inflow angle $\phi(\psi)$ on the advancing side is then expressed as:

$$\phi(\psi) = \tan^{-1}\left(\frac{V_\infty \cos\alpha_P + V_{iA}}{r\Omega + V_\infty \sin\alpha_P \sin\psi - V_{iT}}\right). \tag{1}$$

On the retreating side of the propeller, as depicted in Fig. 2b, where $\pi < \psi < 2\pi$, the in-plane component of the freestream, V_Z, opposes the direction of blade rotation. This opposing direction reduces the tangential velocity, $V_t(\psi) = r\Omega - V_\infty \sin\alpha_P \sin\psi - V_{iT}$, and consequently, the local relative wind speed, $W(\psi)$. The inflow angle is determined by the following relation:

$$\phi(\psi) = \tan^{-1}\left(\frac{V_\infty \cos\alpha_P + V_{iA}}{r\Omega - V_\infty \sin\alpha_P \sin\psi - V_{iT}}\right). \tag{2}$$

Following the BEMT formulation in the axial inflow case [9], the sectional thrust and torque on an annulus of width Δr can be obtained by establishing a BEMT balance for the non-axial inflow case as follows:
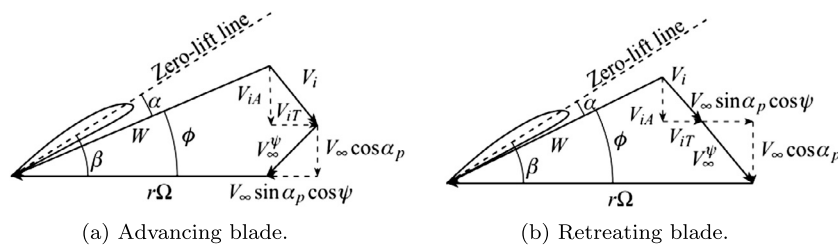
$$\Delta T(\psi, r) = 4\pi r\rho(V_\infty \cos\alpha_P + V_{iA})V_{iA}\Delta r$$
$$= \frac{1}{2}\rho_o W^2 c(C_l \cos\phi - C_d \sin\phi)B\Delta r, \tag{3}$$

$$\Delta Q(\psi, r) = 4\pi r^3 \rho(V_\infty \cos\alpha_P + V_{iA})V_{iT}\Delta r$$
$$= \frac{1}{2}\rho_o W^2 c(C_l \cos\phi + C_d \sin\phi)Br\Delta r, \tag{4}$$

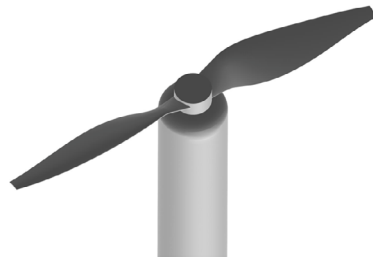where r is the blade radial coordinate, ρ is the fluid density and c is the blade sectional chord, B is the number of blades. The local angle of attack, $\alpha(\psi)$, is determined by the difference between the blade twist angle, β, and the inflow angle, $\phi(\psi)$, such that $\alpha(\psi) = \beta - \phi(\psi)$. The Eqs. (3)-(4) are solved in an iterative procedure with initial guesses for the axial and tangential induced velocities. Upon determining the Reynolds number (Re) and angle of attack seen by a blade element at each ψ, the associated lift and drag coefficients C_l and C_d are interpolated from the 2D meshes of $C_l(\text{Re}, \alpha)$ and $C_d(\text{Re}, \alpha)$ values at each ψ established in a prior step.

The discussion above assumes a quasi-steady condition, implying that the aerodynamic response to changes in inflow angle occurs instantaneously. However, under non-axial inflow, the blade sectional response is delayed due to downwash at the leading edge, reducing lift coefficient and causing a phase lag between inflow variation and aerodynamic response [20]. Accounting for these unsteady effects improves predictions of blade force temporal response and in-plane loads compared to quasi-steady solutions [21,22]. This work applies the Sears function to account for unsteady effects, following a similar approach used in previous work by van Arnhem et al. [22]. This method converts the quasi-steady radial load distributions, given by Eqs. (3)-(4), into the frequency domain and applies corrections using the Sears function. Further details can be found in [22].
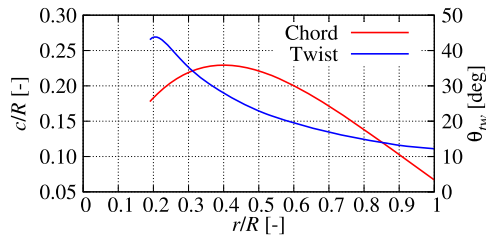
Aeroacoustic calculations are performed by implementing the frequency-domain solution of the convected FW-H equation, as derived by Ghorbaniasl et al. [16]. This formulation explicitly incorporates both aerodynamic and acoustic effects of non-axial inflow. A notable distinction of this formulation, in contrast to the time-domain approach presented in [15], is its freedom from the Doppler singularity and simpler expression of acoustic source terms compared to those of the time-domain formulation. In the following sections, this solver will be referred to as LOPNOR-FWH. The solver operates on a single-core, unlike *Opty∂B*-PNOISE, which, as discussed in the following section, supports concurrent execution across multiple cores. All computations are performed on a laptop equipped with an Intel Core i9 2.3 GHz processor.

2.2. *Opty∂B*

The rotor aeroacoustic L-F model available in *Opty∂B* has been described in [4]. Similarly to LOPNOR, it is based on a BEMT model supplied by *Opty∂B*-BEMT, with sectional aerodynamic polars and boundary layer properties computed with an embedded proprietary viscous panel code based on Drela and Giles' method [23]. The radial distribution of lift and drag coefficients are then converted by *Opty∂B*-PNOISE into constant pressure distributions on the three faces of a radial wedge of the same sectional area of the original blade, following the compact monopole/dipole formulation put forward in [17]. In order to take into account the effects due to sweep/lean angular deflection of the blades, the original definition of the leading- and trailing-edge lines is kept in the surrogate geometrical model of the blade. Moreover, as recently

(a) Advancing blade.

(b) Retreating blade.

Fig. 2. Flow directions of advancing and retreating blade sections [19].

(a) Propeller geometry.

(b) Chord and twist distributions.

Fig. 3. Propeller geometry, airfoil chord and twist spanwise distributions.

shown in [24], the model is able to account for a circumferential variation of the blade geometry and angular spacing, the latter having attracted also the interest of drone rotor researchers [25]. A time-domain acoustic analogy calculation is then applied by automatically executing *Opty∂B*-FOXWHAWK, which makes use of a forward-time formulation of Farassat 1A formulation [26]. This results in periodic noise signals due to the fluid displacement and to the steady loading applied on the blades. In the presence of a non-axial flow, the sectional upwash velocity is evaluated along the rotor revolution, subsequently Fourier-transformed in time, and finally used to calculate an unsteady lift fluctuation by means of a von Kármán-Sears model. The corresponding pressure distribution is added to the steady contribution prior the FW-H calculation. This results in periodic noise signals due to both steady and unsteady loadings applied on the blades. A stochastic inflow turbulence model can be also used to calculate turbulent unsteady loading, but this model is not used in the present study. The noise radiated by the turbulent boundary layer is finally computed by means of a finite-chord thin airfoil semi-analytical model, with leading-edge acoustic back scattering taken into account [27]. A Corcos model is used to estimate the spanwise correlation length, but desingularized in the zero-frequency limit by means of the damping function $1 - e^{-\tilde{\omega}^2/0.09}$, where $\tilde{\omega} = \omega\delta^*/U_e$ is the reduced frequency based on the sectional boundary layer displacement thickness and edge velocity, while the wall-pressure spectra at the trailing edge are computed using a revisited version of Schlinker & Amiet model [28], fed with boundary layer properties extracted at 97.5% and 95.0% of the chord on the suction and pressure side, respectively. The broadband noise spectra are converted into stochastic signal contributions added to the periodic noise signatures.

3. Reference propeller and LB/VLES numerical setup

The geometry herein considered is a two-bladed propeller designed at TU-Delft (Fig. 3a) and extensively examined in previous experimental [29,30] and numerical [4,5,31,6] studies. It is characterized by a radius $R = 0.15$ m and NACA 4412 airfoil sections, which are merged with the propeller hub by elliptical sections (for $r/R < 0.2$). The airfoil chord and twist spanwise distributions are provided in Fig. 3b. The propeller hub radius is 1.25 cm and connected to a nacelle of 5 cm diameter and 52 cm length.

In this work, the propeller is operated at fixed angular velocity ($n = 83.33$ RPS, i.e. $\Omega = 523.6$ rad/s) and $V_\infty = 10$ m/s, resulting in an advance ratio $J = 0.4$ and a BPF of 166.67 Hz. The resulting tip Mach number is 0.23 and the Reynolds number Re based on the chord at 75% of the radius is about $9 \cdot 10^4$. Two different values of the propeller yaw angle are considered to investigate the effects of an angular inflow, namely $\alpha_P = 0°$ and 15°. The free-stream static pressure and temperature considered are $p_\infty = 99000$ Pa and $T_\infty = 293.15$ K, respectively.

H-F simulations have been carried out by means of the commercial CFD software SIMULIA PowerFLOW®. Fig. 4 shows the computational setup [5], which was used to generate the high-fidelity reference data used to validate the L-F methodologies herein proposed. The fluid domain is a spherical volume of $325D$ radius centered around the propeller. Free-stream static pressure and velocity, and turbulence intensity of 0.1% of the free-stream velocity are prescribed on its outer boundary. The experimental anechoic wind tunnel geometry is not modeled in the computational setup. However, an acoustic sponge is used to dissipate the out-going acoustic waves and minimize the backward reflection from the outer boundary, thus reproducing a digital anechoic environment. The acoustic sponge is defined by two concentric spheres of radius $15D$ and $55D$, respectively, centered around the propeller. The fluid kinematic viscosity is gradually increased starting from its physical value within the inner sphere, up to an artificial value two orders of magnitude higher outside the outer one. A zig-zag transition trip is employed on the suction side of the blade to facilitate the VLES scheme transitioning from a scale-modeling to scale-resolving behavior, thus allowing the formation of turbulent structures within the boundary layer causing trailing-edge noise radiation. The zig-zag trip is characterized by a thickness of 0.17 mm, amplitude and wavelength of 0.9 mm, and is located at 25% of the chord on the suction side of the blade for $r/R > 0.2$ (Fig. 4). No trip is used on the blade pressure side, since no laminar-to-turbulent boundary layer transition is expected to occur based on the *Opty∂B*-BEMT computations. This approach has been successfully validated in previous studies on the prediction of the performances and tonal/broadband noise radiation of a low-speed propeller in axial and non axial inflow conditions [4,32,5]. It is worth mentioning that these simulations have been performed before the introduction of a new VLES model in PowerFLOW that, when the mesh resolution is sufficiently high, promotes a spontaneous transition between modeled to resolved turbulence [31] in the boundary layer, without the need of a physical trip. This new model is also key to predict the occurrence of laminar separation bubbles.

Fig. 4 shows the details of the computational setup and grid close to the propeller geometry. The propeller and hub are encompassed by a volume of revolution that defines the Local Reference Frame (LRF), i.e. the rotating sliding mesh domain used to enable the propeller rotation. The solid FW-H integration surface used to compute the far-field noise radiation coincides with the propeller, hub and nacelle surfaces. A total of 16 Variable Resolution (VR) regions are used to discretize the whole fluid domain, with the finest resolution level (VR15) placed around the blade trip and trailing-edge. A resolution of 200 voxels along the mean chord (22.85 mm) is used in the second finest resolution level (VR14), resulting in a smallest voxel size of 0.06 mm, a mean $y^+ \simeq 5$ on the blade surface and an overall mesh size of 107 million voxels. The computational cost is 840 CPUh/rev on a 430 cores cluster with Intel Xeon CPU E5-2697 2.6 GHz. The whole fluid domain is initialized with the instantaneous flow solution from a statistically converged coarser simulation. Hence, after a settling time corresponding to 2 propeller revolutions, the sampling of relevant flow data is started for 10 additional revolutions. Acoustic data is sampled at 365 kHz with spatial averaging of 0.5 mm on the solid FW-H integration surface. Fourier transformed data is obtained with 2 Welch blocks, 50% overlap and Hanning windowing, corresponding to a bandwidth of 16.6 Hz (BPF 0.1).
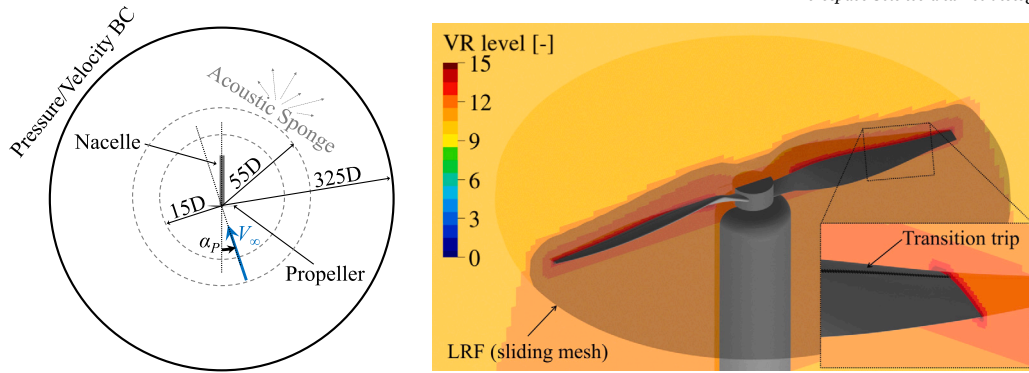
Fig. 4. Sketch of computational setup (left, not drawn to scale) and near body grid (right). (For interpretation of the colors in the figure(s), the reader is referred to the web version of this article.)
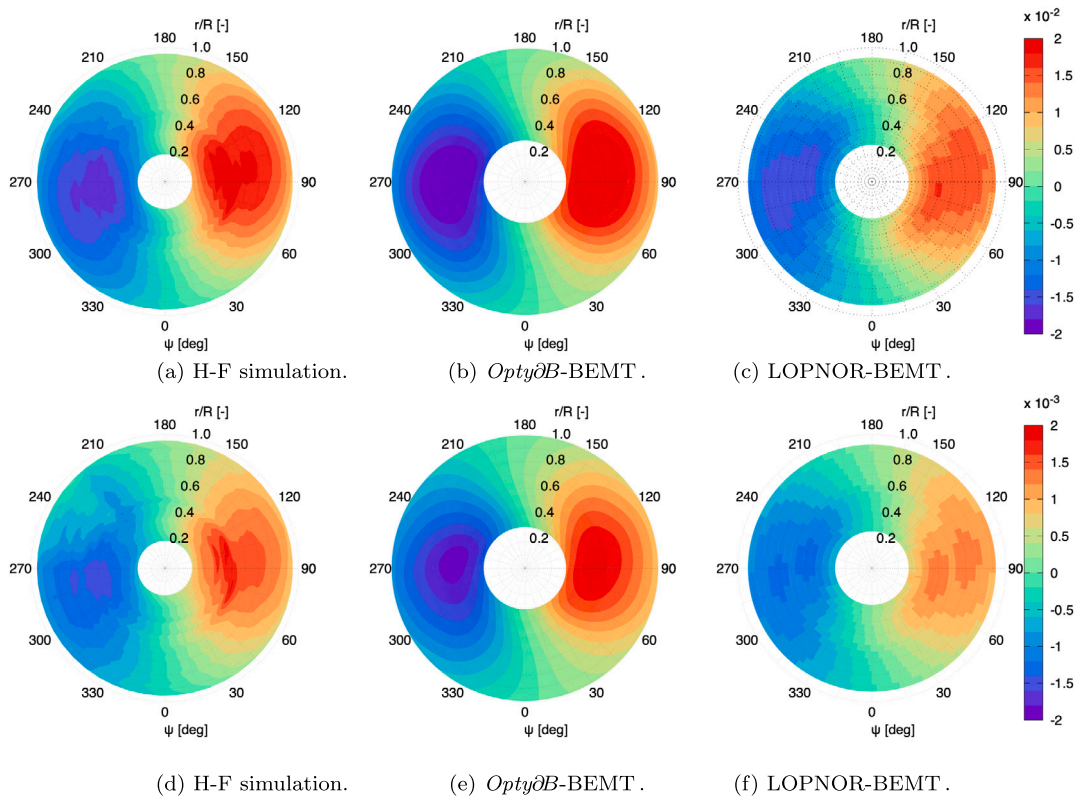

(a) H-F simulation. (b) $Opty\partial B$-BEMT. (c) LOPNOR-BEMT.

(d) H-F simulation. (e) $Opty\partial B$-BEMT. (f) LOPNOR-BEMT.

Fig. 5. Fluctuating thrust (top) and torque (bottom) coefficient for the $\alpha_P = 15°$ case.

4. Results

4.1. Unsteady thrust and torque distributions on the rotor disk

The L-F prediction capabilities of the unsteady thrust and torque distributions on the rotor disk are investigated by comparing results with reference H-F data. The fluctuating, mean-removed, sectional thrust and torque distributions, $C'_{\partial rT}$ and $C'_{\partial rQ}$, are compared in Fig. 5. As expected, due to the non-axial flow condition, a classical 1-rev asymmetric pattern of the disk loading is obtained. More specifically, two distinctive features are visible in both the H-F and L-F results. First, the highest and lowest values occur slightly after $\psi = 90°$ and $\psi = 270°$, respectively. This is due to the delayed blade aerodynamic response to the upwash velocity variation that, in the L-F methods, is taken into account by the unsteady aerodynamics airfoil response. Second, variations on the advancing side are higher than those on the retreating side, primarily due

to the larger increase in the local airfoil angle of attack on the advancing side compared to its reduction on the retreating side [5]. Both L-F approaches capture these features.

The H-F results exhibit the presence of some irregularities that are attributed to the following aspects. The first one is the presence of the trip in the simulations, which generates local flow fluctuations and makes the sectional load extraction more difficult. The second is related to the sectional load extraction procedure that was not very robust at the time when these loads were evaluated. A new procedure is currently in place and it will be used in future to update these results.

Finally, it is interesting to notice that both the H-F and the LOPNOR-BEMT torque distributions exhibit a double main lobe pattern, with a small drop around $r/R = 0.5$. This pattern is not visible in the $Opty\partial B$-BEMT results. Due to the presence of the aforementioned artifacts in the H-F loading extraction procedure, it is not meaningful to speculate on the physical nature of this feature at the present stage.
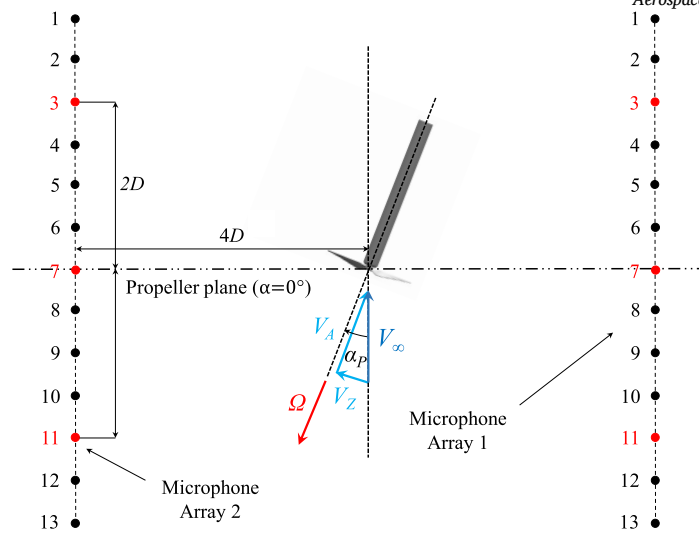
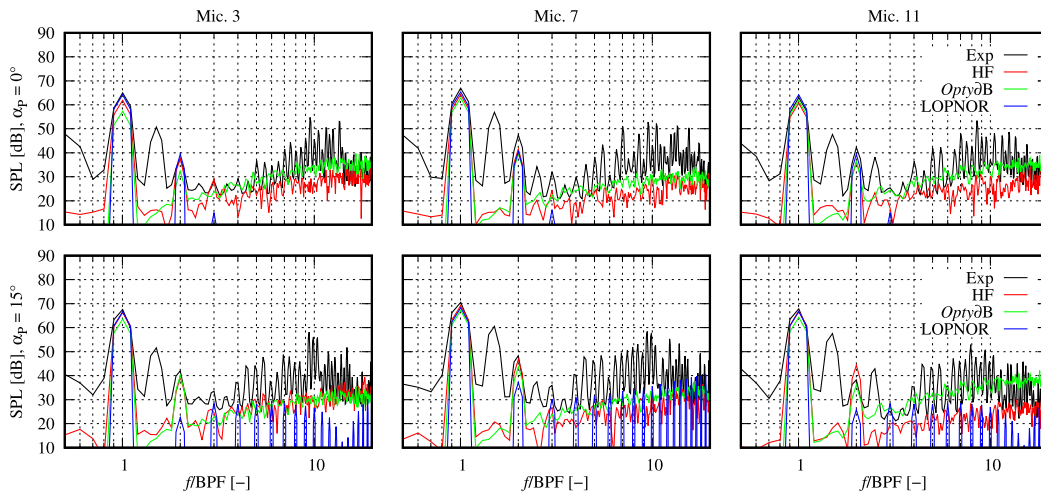**Fig. 6.** Sketch of the microphone array used of far-field noise computation.

Fig. 7. Far-field noise spectra at three microphones on array 1 and both axial (top) and non-axial flow conditions (bottom).

4.2. Far-field noise spectra

The L-F prediction capabilities of far-field noise are examined in this subsection by comparing the L-F results against the H-F results and the wind tunnel measurements. As illustrated in Fig. 6, three different microphones, vertically aligned along two opposite linear arrays, are considered: Mic. 3, located at (0.6, 1.2, 0.0) m in a free-stream and hub-centered reference system, and Mic. 11 (-0.6, 1.2, 0.0) m are positioned outside the untitled propeller plane ($\alpha_P = 0°$), while Mic. 7 (0.0, 1.2, 0.0) m is located within the untitled propeller plane.

The far-field noise spectra are computed for all microphones on array 1 for both axial and angular inflow cases and compared against data from H-F and experimental measurements, as shown in Fig. 7. For $\alpha_P = 0°$, at Mic. 3, LOPNOR shows good agreement with the measurements at the first and second BPF harmonics, while $Opty\partial B$ underpredicts the tonal peaks at both BPF harmonics. At Mic. 7, both LOPNOR and $Opty\partial B$ show good agreement at the first BPF with both measurements and H-F data, but they underpredict the tonal peaks of the second BPF compared to the measurements, while showing good agreement with the H-F data. At Mic. 11, both L-F predictions exhibit a very good agreement with the measurements and the H-F data at both BPF harmonics. For all microphones, $Opty\partial B$ shows a fairly good agreement with the H-F results across the whole frequency range. In contrast, LOPNOR only shows emerging tonal peaks up to the third harmonics, with significantly lower

values at the third BPF harmonic due to its lack of broadband noise calculation capability. This limitation will be addressed in future studies. For $\alpha_P = 15°$, an overall increase in noise levels at all microphones is observed compared to $\alpha_P = 0°$, particularly at Mic. 7. LOPNOR shows excellent agreement with both the measurements and H-F data for the first BPF at all microphones. In contrast, $Opty\partial B$ slightly underpredicts the tonal peaks at the first BPF. At the second BPF, LOPNOR significantly underpredicts the tonal peaks at Mic. 3 and Mic. 7, although this underprediction is slightly less pronounced at Mic. 7. Conversely, $Opty\partial B$ shows excellent agreement with the measurement data at the second harmonics of the BPF across all microphones. Unlike for the axial inflow condition, LOPNOR predicted the tonal peaks at the third BPF reasonably well compared to the measurements. It also shows good agreement with the H-F data at Mic. 3 and Mic. 7, it slightly overpredicts the H-F results at Mic. 11, while maintaining excellent agreement with the measurement data. Similarly, $Opty\partial B$ shows good agreement with the H-F data across all higher harmonics at Mic. 3, fairly good agreement at Mic. 7, and an overprediction at Mic. 11. Notably, LOPNOR shows very good agreement with $Opty\partial B$ and reasonable agreement with the H-F data across all harmonics at Mic 7, while a poorer prediction at Mic. 3 and Mic. 11. This suggests that tonal noise due unsteady loading becomes a significant contributor at higher harmonics.

The far-field noise spectra at microphones distributed on array 2 are shown in Fig. 8. For axial inflow conditions, similar trends as for the
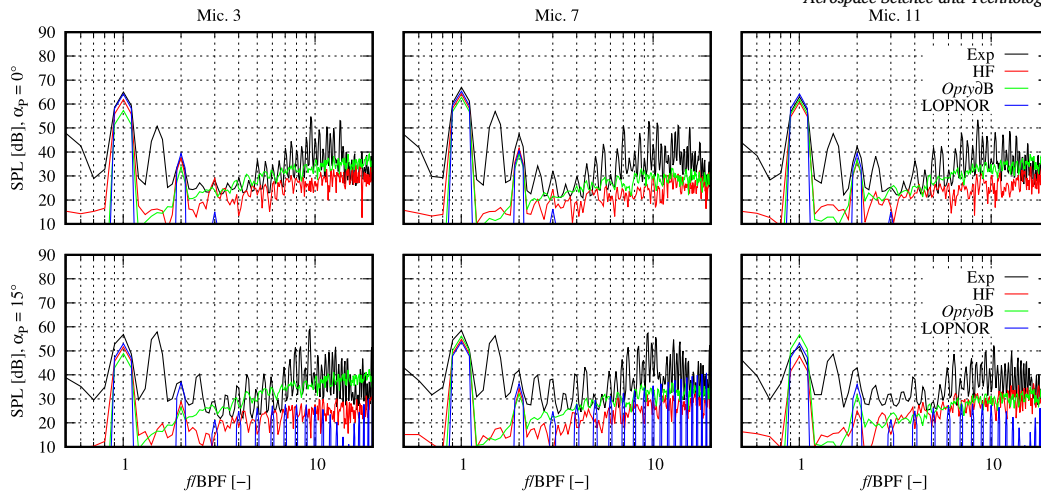
Fig. 8. Far-field noise spectra for three microphones on array 2 and both axial (top) and non-axial flow conditions (bottom).

microphones on array 1 can be observed, and in particular some underpredictions of the BPF harmonics compared to measurements likely due to the presence of additional unsteadiness in the experiments due to flow recirculation in the test chamber, and globally a slightly better agreement with the H-F results. Moreover, the *Opty∂B* results confirm a fair broadband noise prediction capability.

It should be noted that measurements at all microphones exhibit significant tonal peaks at BPF 0.5, 1.5, and 2.5. These peaks are attributed to an imperfect balance of the blade loading on the two blades in the test rig. This mechanism is not present in the simulations since a perfectly symmetric rotor is considered.

Although tracking the specific reasons of discrepancy in tone level prediction is not the final goal of this work, it should be also mentioned that the H-F results have been obtained by neglecting the mean-flow convection effects, under the assumption that the sound propagation mostly occurs in quiescent conditions outside the wind-tunnel jet. On the contrary, the L-F predictions take into account a free-stream convection. As a matter of fact, comparisons between H-F and *Opty∂B* results for the same rotor in hover conditions and higher rotational speed carried out in [33] exhibit an almost perfect agreement of tonal levels.

As a conclusive remark of this subsection, it is worth arguing that, in general, rotor noise tones are submitted to several uncertainties, both in measurements and predictions. Therefore, a meaningful one-to-one tonal level comparison would require a characterization of the uncertainties associated with every process, as recently pointed out in [33].

4.3. Noise power level

The investigation of the L-F prediction capabilities of propeller noise at incidence is concluded with the calculation of the noise power level (PWL). This represents the acoustic energy generated by the propeller, independently of distance and observation angle. The PWL spectrum is evaluated by integrating the power spectral densities (PSD) of the noise computed at microphones distributed on a spherical array of radius of 10R, centered around the propeller hub, using the following formula [5]:

$$\mathrm{PWL}(f) = \int_0^\pi \int_0^{2\pi} R_s^2 \sin(\theta) \frac{[1 + M_\infty \cos(\theta)]^2 \mathrm{PSD}(f, \eta, \theta)}{2\rho_0 c_0} \, d\eta \, d\theta, \quad (5)$$

where f is the frequency, R_s is the sphere radius, and θ and η are the latitudinal and longitudinal angular coordinates, respectively, with the free-stream being directed from the northern ($\theta = 0°$) to the southern ($\theta = 180°$) pole of the sphere. A total of 375 microphones, equally distributed along 15 parallel (i.e. θ coordinate) and 25 meridian (i.e. η coordinate) points, have been used.

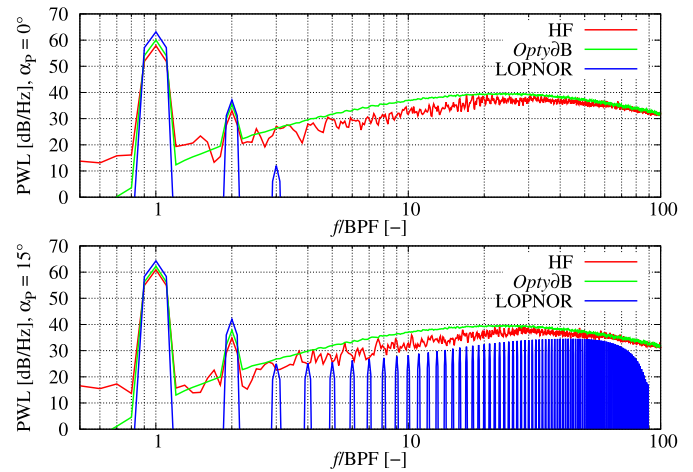**Fig. 9.** Comparison between Power Watt Level (PWL) spectra from H-F simulation, *Opty∂B* and LOPNOR for $\alpha_P = 0°$ and $\alpha_P = 15°$.

The PWLs computed with both L-F solvers are compared against H-F data for axial ($\alpha_P = 0°$) and angular inflow ($\alpha_P = 15°$) conditions, as depicted in Fig. 9. For the axial inflow condition, both LOPNOR and *Opty∂B* slightly overpredict the first BPF tone compared to the H-F results, while showing a much better agreement at the second BPF. Notably, *Opty∂B* exhibits excellent agreement with H-F data across the entire frequency range. Under the angular inflow condition ($\alpha_P = 15°$), predictions at the first BPF improve significantly compared to the axial inflow condition. However, LOPNOR overpredicts the H-F result at the second BPF, whereas this overprediction is smaller with *Opty∂B*, which shows a better overall agreement with the H-F data compared to LOPNOR.

The PWL predictions suggest that noise emissions of the propeller at incidence are accurately predicted by both L-F approaches, which can be therefore used for rotor noise prediction at incidence, with significantly reduced computation time compared to H-F calculations, as detailed in Table 1. The CPU time for the broadband *Opty∂B*-PNOISE calculation includes the noise spectra calculation and the broadband signal auralization prior merging of the tonal and broadband signals. This second step, which is indeed an optional one, is the most expensive part of the broadband noise signals calculation. Moreover, in order to have a high frequency sampling of the synthetic broadband noise signals, the *Opty∂B*-PNOISE calculations were performed with 500 time-steps per blade passing period. For the sake of consistency, the same time step was used for the tonal noise calculations. Since a much lower value would be sufficient to recover the proper tonal noise levels, the reported CPU time

Table 1

Comparison of CPU time between LOPNOR-FWH and *Opty∂B*-PNOISE for 375 microphones. T indicates tonal component, while B represents broadband component.

Solver	α_P	# CPU cores	CPU time (T) [s]	CPU time (B) [s]
Opty∂B-PNOISE	0°	10	57	914
LOPNOR-FWH	0°	1	40	N/A
Opty∂B-PNOISE	15°	10	64	924
LOPNOR-FWH	15°	1	12204	N/A

for tonal noise calculations are much higher than what is really needed for pure tonal noise predictions. On the other hand, the CPU time of LOPNOR-FWH for the axial flow condition reflects a reasonable computational time for a frequency-domain solver typically used for propeller tonal noise calculations, considering only three harmonics. However, for the non-axial case, the CPU time increased significantly due to the consideration of 101 harmonics to cover the full frequency range, ensuring consistency with the other two predictions on the PWL noise calculation. Therefore, a direct comparison of CPU time with *Opty∂B*-PNOISE for the non-axial condition does not reflect reality. Nevertheless, it is interesting to report these CPU time figures for the sake of future reference.

5. Conclusion

The accuracy and computational efficiency of two low-fidelity methods for propeller tonal and broadband noise prediction in both axial and non-axial flow scenarios were investigated. Experimental data and scale-resolving LB/VLES CFD results for a two-bladed small unmanned aerial system under transitional boundary layer conditions were used as a reference. The following conclusions are drawn:

- The comparison of unsteady loading predictions indicates that, both L-F approaches provide satisfactory predictions of the unsteady thrust and torque distribution on the rotor disk in non-axial flow conditions.
- For far-field noise spectra predictions, both L-F approaches show excellent agreement with high-fidelity and measurement data in axial conditions. *Opty∂B* accurately predicts broadband noise at higher harmonics, while LOPNOR lacks this capability. In non-axial conditions, both methods capture significant increases and decreases in noise levels at the first harmonics of BPF across all microphones. However, LOPNOR systematically underpredicts the tonal peak at the second BPF on array 1, while *Opty∂B* does so on array 2.
- Under non-axial conditions, tonal noise from unsteady loading can substantially contribute to the lower to mid frequency range, comparable to other broadband noise sources in this range.
- *Opty∂B* accurately predicts PWL at all frequencies with slight over-prediction up to the 11th BPF, while LOPNOR accurately predicts the first two BPF tonal peaks in axial conditions. However, for non-axial conditions, LOPNOR considerably overpredicts the second BPF, while capturing the trend at higher harmonics.
- For the tonal noise calculation, the two low-fidelity approaches exhibit similar computational costs.

The results suggest that both approaches can be effectively utilized for predicting tonal noise of propellers under non-axial inflow conditions with acceptable accuracy and significant reduction in computation time compared to H-F predictions. Additionally, *Opty∂B* can be employed to predict broadband noise across the entire frequency range. The dominance of tonal noise from unsteady loading in the lower to mid-frequency range, compared to broadband noise sources, will be investigated in future work.

Finally, new LB/VLES high-fidelity simulations will be performed in the future using a recently released extension of the PowerFLOW VLES model [31,6], which was developed to address low-Reynolds number flows, to incorporate the effects of the laminar separation bubble on the aerodynamic loading and thus providing a more reliable benchmark for the assessment of the L-F methodologies.

CRediT authorship contribution statement

Furkat Yunus: Writing – review & editing, Writing – original draft, Visualization, Validation, Software, Methodology, Investigation, Formal analysis, Conceptualization. **Damiano Casalino:** Writing – review & editing, Validation, Supervision, Software, Conceptualization. **Gianluca Romani:** Writing – review & editing, Visualization, Validation, Data curation. **Mirjam Snellen:** Writing – review & editing, Supervision, Project administration, Funding acquisition.

Declaration of competing interest

The authors declare that they have no known competing financial interests or personal relationships that could have appeared to influence the work reported in this paper.

Data availability

No data was used for the research described in the article.

References

[1] B. Magliozzi, D. Hanson, R. Amiet, Propeller and propfan noise, in: H.H. Hubbard (Ed.), Aeroacoustics of Flight Vehicles: Theory and Practice, NASA, 1991, pp. 1–64.

[2] T. Zhang, G.N. Barakos, A. Filippone, Furqan, High-fidelity aero-acoustic evaluations of a heavy-lift eVTOL in hover, J. Sound Vib. 584 (2024) 118453, https://doi.org/10.1016/j.jsv.2024.118453.

[3] T. Brooks, D. Pope, M. Marcolini, Airfoil self-noise and prediction, NASA Reference Publication 1218, NASA, 1989.

[4] D. Casalino, E. Grande, G. Romani, D. Ragni, F. Avallone, Definition of a benchmark for low Reynolds number propeller aeroacoustics, Aerosp. Sci. Technol. 113 (2021) 106707.

[5] G. Romani, E. Grande, F. Avallone, D. Ragni, D. Casalino, Computational study of flow incidence effects on the aeroacoustics of low blade-tip Mach number propellers, Aerosp. Sci. Technol. 120 (2022) 107275.

[6] D. Casalino, G. Romani, L.M. Pii, R. Colombo, Flow confinement effects on sUAS rotor noise, Aerosp. Sci. Technol. 143 (2023) 108756.

[7] J. Goyal, T. Sinnige, C.S. Ferreira, F. Avallone, Aerodynamics and far-field noise emissions of a propeller in positive and negative thrust regimes at non-zero angles of attack, in: AIAA AVIATION 2023 Forum, 2023, p. 3217.

[8] D. Casalino, W.C. van der Velden, G. Romani, Community noise of urban air transportation vehicles, in: AIAA Scitech 2019 Forum, 2019, p. 1834.

[9] F. Yunus, B. von den Hoff, M. Snellen, Predicting tonal noise of full-electric propeller-driven aircraft in outdoor environments using low-order models, in: 30th AIAA/CEAS Aeroacoustics Conference (2024), 2024, p. 3418.

[10] F. Yunus, E. Grande, D. Casalino, F. Avallone, D. Ragni, Efficient low-fidelity aeroacoustic permanence calculation of propellers, Aerosp. Sci. Technol. 123 (2022) 107438.

[11] M.H. McCrink, J.W. Gregory, Blade element momentum modeling of low-Reynolds electric propulsion systems, J. Aircr. 54 (1) (2017) 163–176.

[12] R. MacNeill, D. Verstraete, Blade element momentum theory extended to model low Reynolds number propeller performance, Aeronaut. J. 121 (1240) (2017) 835–857.

[13] D. Usov, W. Appleton, A. Filippone, N. Bojdo, Low-order aerodynamic model for interference in multirotor systems, J. Aircr. 59 (6) (2022) 1450–1462, https://doi.org/10.2514/1.C036797.

[14] F. Farassat, M. Dunn, P. Spence, Advanced propeller noise prediction in the time domain, AIAA J. 30 (9) (1992) 2337–2340.

[15] G. Ghorbaniasl, C. Lacor, A moving medium formulation for prediction of propeller noise at incidence, J. Sound Vib. 331 (1) (2012) 117–137.

[16] G. Ghorbaniasl, Z. Huang, L. Siozos-Rousoulis, C. Lacor, Analytical acoustic pressure gradient prediction for moving medium problems, Proc. R. Soc. A, Math. Phys. Eng. Sci. 471 (2184) (2015) 20150342.

[17] D. Casalino, M. Barbarino, A. Visingardi, Simulation of helicopter community noise in complex urban geometry, AIAA J. 48 (8) (2011) 1614–1624.

[18] M. Drela, Xfoil: an analysis and design system for low Reynolds number airfoils, in: Low Reynolds Number Aerodynamics: Proceedings of the Conference Notre Dame, Indiana, USA, 5–7 June 1989, Springer, 1989, pp. 1–12.

[19] Y. Leng, T. Jardin, J.-M. Moschetta, M. Bronz, Analytic model of proprotor forces and moments at high incidence, J. Am. Helicopter Soc. 66 (4) (2021) 1–15.

[20] W.R. Sears, Some aspects of non-stationary airfoil theory and its practical application, J. Aeronaut. Sci. 8 (3) (1941) 104–108.

[21] F. Yunus, D. Casalino, G. Romani, M. Snellen, Efficient prediction of propeller noise at incidence, in: Quite Drones Symposium (2024), Manchester, UK, 2024.

[22] N. van Arnhem, R. de Vries, T. Sinnige, R. Vos, G. Eitelberg, L.L. Veldhuis, Engineering method to estimate the blade loading of propellers in nonuniform flow, AIAA J. 58 (2020) 5332–5346, https://doi.org/10.2514/1.J059485.

[23] M. Drela, M.B. Giles, Viscous-inviscid analysis of transonic and low Reynolds number airfoils, AIAA J. 25 (10) (1987) 1347–1355.

[24] L.M. Pii, D. Casalino, G. Romani, K. Singal, Aeroacoustic optimization of an axial cooling fan with fundamental observations, in: 30th AIAA/CEAS Aeroacoustics Conference, 2024.

[25] D. Usov, D. Koning, T. Chronis, A. Filippone, D. Akiwate, A.J. Torija Martinez, Aerodynamics and acoustics of asymmetric propellers with uneven blade spacing, in: 30th AIAA/CEAS Aeroacoustics Conference (2024), 2024, p. 3265.

[26] D. Casalino, An advanced time approach for acoustic analogy predictions, J. Sound Vib. 261 (4) (2003) 583–612.

[27] M. Roger, S. Moreau, Back-scattering correction and further extensions of Amiet's trailing edge noise model, part 1: theory, J. Sound Vib. 286 (3) (2005) 477–506.

[28] R.H. Schlinker, R.K. Amiet, Helicopter rotor trailing edge noise, NASA Contractor Report 3074, NASA, 1981.

[29] E. Grande, G. Romani, D. Ragni, F. Avallone, D. Casalino, Aeroacoustic investigation of a propeller operating at low Reynolds numbers, AIAA J. 60 (2) (2022) 860–871.

[30] E. Grande, D. Ragni, F. Avallone, D. Casalino, Laminar separation bubble noise on a propeller operating at low Reynolds numbers, AIAA J. 60 (9) (2022) 5324–5335.

[31] D. Casalino, G. Romani, R. Zhang, H. Chen, Lattice-Boltzmann calculations of rotor aeroacoustics in transitional boundary layer regime, Aerosp. Sci. Technol. 130 (2022) 107953.

[32] G. Romani, E. Grande, F. Avallone, D. Ragni, D. Casalino, Performance and noise prediction of low-Reynolds number propellers using the lattice-Boltzmann method, Aerosp. Sci. Technol. 125 (2022) 107086.

[33] L.T. Lima Pereira, D. Ragni, G. Romani, D. Casalino, Accuracy of tonal noise prediction of propellers via numerical simulations and experimental campaigns, in: 30th AIAA/CEAS Aeroacoustics Conference (2024), 2024, p. 3267.